AerospaceEurope Conference2021
WARSAW, POLAND | 23 -26 NOVEMBER 2021
CEAS Council of European Aerospace Societies
PSAA

Quadrotor motion analysis and control in wind environment

Robert Głębocki[1], Mariusz Jacewicz[2]

[1]Institute of Aeronautics and Applied Mechanics, Warsaw University of Technology, 00-665 Warsaw, Poland; robert.glebocki@pw.edu.pl
[2]Institute of Aeronautics and Applied Mechanics, Warsaw University of Technology, 00-665 Warsaw, Poland; mjacewicz@meil.pw.edu.pl

Abstract

One of the main drawbacks of quadrotors is high energy consumption which limits the flight duration. To plan the quadrotor mission effectively the energy expenditure should be predicted. The purpose of the study was to create a high-fidelity energy consumption model for a low-cost quadrotor. Six degree of freedom mathematical model was developed, implemented into MATLAB/Simulink and validated using real flight trials data. DJI Mavic 2 Pro drone was used as a test platform. It was obtained that the model allows predicting accurately the drone flight parameters, the amount of consumed energy, state of charge of the onboard battery, and voltage level. The developed numerical simulation might be used for planning real object missions.

Keywords: quadrotor; energy consumption; model validation

1. Introduction

In the last years, quadrotors become very popular and used in a wide area of applications, e.g. agricultural, aerial imaging, search & rescue missions, package delivery, reconnaissance, inspection, etc. [1], [2]. Vertical take-off and landing capability, high maneuverability, relatively simple mechanical design, and low cost gives them advantages over fixed-wing drones and helicopters. They are often powered by Lithium-Ion multiple-use batteries. These batteries offer high energy density, lack of memory effects, and low mass.

One of the main problems with quadrotors is limited energy available onboard, quite a large energy consumption, and resulting short time of flight duration. A large amount of energy is spent to maintain the drone in the air. To maximize flight efficiency the mission should be planned carefully. To realize this goal a reliable mathematical model of the energy consumption by the drone in various flight conditions is necessary.

The topic of electrical energy consumption by the quadrotors was previously studied by several researchers. Yacef et all. [3], [4] studied the energy consumption of the quadrotor and presented the mathematical models of electric motors. Sheng and Sun [5] analyzed the usage of variable pitch propellers to minimize drone power consumption. Agarwal and Tewari [6] investigated the use of reinforcement learning to optimize energy expenditure. Energy-efficient path-planning with the aim of the genetic algorithm was studied by Shivgan and Dong in [7]. Pradeep et all. [8] analyzed the energy consumption in the monitoring mission. Jee and Cho [9] studied the energy consumption in various flight patterns. Gao et all. [10] validated the theoretical energy model for a quadrotor. Dietrich et all. [11] presented analysis of energy consumption and proposed empirical formula to predict the consumed energy. An empirical model of energy consumption was presented by Abeywickrama et all. [12]. The energy consumption model was shown by Korneyev et all. in [13]. Hwang et all. [14] presented method for estimation of endurance of flight. Wang et all. [15] discussed analytical power consumption model. Aleksandrov and Penkov [16] presented the

theoretical energy calculation for quadrotors with the different number of rotors. Chen et all. [17] described battery-aware model for prediction of energy consumed by the drone. Apeland et all. [18] discussed the model of the fuel cell. Prasetia et all. [19] proposed black-box modeling of energy consumption. Rodrigues et all. [20] presented a data-set suitable for energy consumption research. Roberts et all. [22] proposed endurance estimation model. Chan and Kam [23] showed a procedure for energy consumption estimation. The simple endurance model was presented by Abdilla et all. [24]. Power consumption measurements were shown by Penkov and Aleksandrov [25].
The goal of the presented study was to develop and validate the reliable simulation model of energy consumption by the quadrotor in the typical mission.
The main contribution of this paper is the comparison of calculated results with the data from real flight tests in windy environment.
The structure of the paper is as follows. In Section 2 the test platform and nonlinear mathematical model of the object are presented. The assumed autopilot structure and energy consumption model are also described. In Section 3 flight tests are explained and model validation is shown. This manuscript ends with a discussion of obtained results and a summary of the main findings.

2. Materials and Methods

2.1 Test platform

Commercially available DJI MAVIC 2 Pro [26] quadcopter was used as a test mobile platform. The drone (Figure 1) possesses cross-configuration and was modified to integrate the object with the pads of the ground charging station (e.g. legs were added). The total mass of the drone after several modifications is m = 0.960 [kg] and moments of inertia are: I_{xx} = 0.00010246 [kgm^2], I_{yy} = 0.00007672 [kgm^2], I_{zz} = 0.0000053043 [kgm^2]. Mass of the drone was evaluated through measurements. The moments of inertia were estimated experimentally using trifilar pendulum methodology. Products of inertia I_{xy}, I_{yz}, I_{zx} were assumed to be negligible.

Figure 1 – DJI MAVIC 2 Pro (front view).

The diameter of the single propeller is R_d = 0.22 [m]. Propellers number 1 (forward right) and 3 (aft left) rotate counterclockwise looking from the top whereas 2 (aft right) and 4 (forward left) spin clockwise. The object is equipped with a gimbaled camera and several onboard sensors. A set of flight data parameters could be recorded during the mission using the build-in functionality.

2.2 Model assumptions

It was assumed that the quadrotor is a rigid body with 6 degrees of freedom (DOF) and constant mass. Aerodynamic interference between rotors and fuselage was neglected. The motor dynamic was included in the model. Earth rotation effects were neglected. Gravity acceleration g was calculated using WGS-84 model. Air density was obtained according to ISA Atmosphere model [27]. Wind field was incorporated into the simulation.

2.3 Coordinate frames

In Figure 2 the coordinate systems used in the mathematical model are shown.

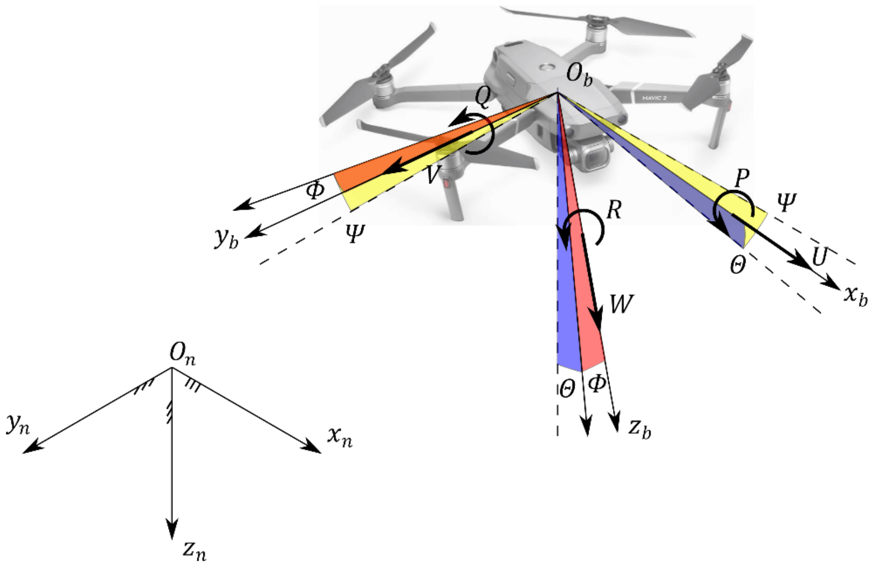

Figure 2 – Coordinate systems used in the model.

$O_n x_n y_n z_n$ is Earth fixed North-East-Down oriented coordinate frame. $O_b x_b y_b z_b$ is a frame rigidly attached to the quadrotor that moves with the object. Origin O_b is located at the center of mass of the drone, $O_b x_b$ axis is pointed forward, $O_b y_b$ on right and $O_b z_b$ is pointed down.

The state vector of the system is:

$$\boldsymbol{x_{state}} = [U \quad V \quad W \quad P \quad Q \quad R \quad x_n \quad y_n \quad z_n \quad \Phi \quad \Theta \quad \Psi]^T \tag{1}$$

where: U, V, W – linear quasi-velocities in $O_b x_b y_b z_b$ frame, P, Q, R – quasi-angular rates in $O_b x_b y_b z_b$ frame, x_n, y_n, z_n – position coordinates in $O_n x_n y_n z_n$ frame, Φ, Θ, Ψ – roll, pitch, and yaw angles, respectively.

The z_n is the vertical coordinate which relates to the altitude h by:

$$h = -z_n \tag{2}$$

The transformation matrix from $O_b x_b y_b z_b$ to $O_n x_n y_n z_n$ is:

$$\boldsymbol{T_b^n} = \begin{bmatrix} \cos\Theta\cos\Psi & \sin\Phi\sin\Theta\cos\Psi - \cos\Phi\sin\Psi & \cos\Phi\sin\Theta\cos\Psi + \sin\Phi\sin\Psi \\ \cos\Theta\sin\Psi & \sin\Phi\sin\Theta\sin\Psi + \cos\Phi\cos\Psi & \cos\Phi\sin\Theta\sin\Psi - \sin\Phi\cos\Psi \\ -\sin\Theta & \sin\Phi\cos\Theta & \cos\Phi\cos\Theta \end{bmatrix} \tag{3}$$

Quaternions were used to describe the attitude of the object:

$$e_0^2 + e_1^2 + e_2^2 + e_3^2 = 1 \tag{4}$$

To improve the accuracy of the numerical calculation and ensure the satisfaction of equation (4) method of algebraic constraint is used [28]. The kinematic constraints are then given as follows [29]:

$$\begin{bmatrix} \dot{e}_0 \\ \dot{e}_1 \\ \dot{e}_2 \\ \dot{e}_3 \end{bmatrix} = -\frac{1}{2} \begin{bmatrix} 0 & P & Q & R \\ -P & 0 & -R & Q \\ -Q & R & 0 & -P \\ -R & -Q & P & 0 \end{bmatrix} \begin{bmatrix} e_0 \\ e_1 \\ e_2 \\ e_3 \end{bmatrix} - kE \begin{bmatrix} e_0 \\ e_1 \\ e_2 \\ e_3 \end{bmatrix} \tag{5}$$

where: k – constant coefficient, E – constraint (E = 0 in an ideal situation) which is given as [28]:

$$E = e_0^2 + e_1^2 + e_2^2 + e_3^2 - 1 \tag{6}$$

The coefficient k is often chosen empirically to ensure $kh_{int} \leq 1$, where h_{int} is numerical integration step [29] (it was assumed that k = 1). The integration in time of (5) allows obtaining quaternion e_0, e_1, e_2, e_3 that describes the attitude.

The kinematic relations between position coordinates in $O_n x_n y_n z_n$ frame and quasi-velocities in $O_b x_b y_b z_b$ are [28], [29], [30]:

$$\begin{bmatrix} \dot{x}_n \\ \dot{y}_n \\ \dot{z}_n \end{bmatrix} = \boldsymbol{\Lambda} \begin{bmatrix} U \\ V \\ W \end{bmatrix} \tag{7}$$

where $\boldsymbol{\Lambda}$ is defined as:

$$\boldsymbol{\Lambda} = \begin{bmatrix} e_0^2 + e_1^2 - e_2^2 - e_3^2 & 2(e_1 e_2 - e_0 e_3) & 2(e_0 e_2 + e_1 e_3) \\ 2(e_0 e_3 + e_1 e_2) & e_0^2 - e_1^2 + e_2^2 - e_3^2 & 2(e_2 e_3 - e_0 e_1) \\ 2(e_1 e_3 - e_0 e_2) & 2(e_0 e_1 + e_2 e_3) & e_0^2 - e_1^2 - e_2^2 + e_3^2 \end{bmatrix} \tag{8}$$

For post-processing purposes, the Euler angles were calculated as [28], [31]:

$$\Phi = \operatorname{atan}\left[\frac{2(e_0 e_1 + e_2 e_3)}{e_0^2 - e_1^2 - e_2^2 + e_3^2}\right] \tag{9}$$

$$\Theta = \operatorname{asin}[2(e_0 e_2 - e_1 e_3)] \tag{10}$$

$$\Psi = \operatorname{atan}\left[\frac{2(e_0 e_3 + e_1 e_2)}{e_0^2 + e_1^2 - e_2^2 - e_3^2}\right] \tag{11}$$

To integrate (5) it is necessary to calculate initial quaternion values. Initial altitude was defined by Euler angles Φ, Θ, Ψ, and then recalculated on quaternions as [28], [31]:

$$e_0 = \cos\frac{\Phi}{2}\cos\frac{\Theta}{2}\cos\frac{\Psi}{2} + \sin\frac{\Phi}{2}\sin\frac{\Theta}{2}\sin\frac{\Psi}{2} \tag{12}$$

$$e_1 = \sin\frac{\Phi}{2}\cos\frac{\Theta}{2}\cos\frac{\Psi}{2} - \cos\frac{\Phi}{2}\sin\frac{\Theta}{2}\sin\frac{\Psi}{2} \tag{13}$$

$$e_2 = \cos\frac{\Phi}{2}\sin\frac{\Theta}{2}\cos\frac{\Psi}{2} + \sin\frac{\Phi}{2}\cos\frac{\Theta}{2}\sin\frac{\Psi}{2} \tag{14}$$

$$e_3 = \cos\frac{\Phi}{2}\cos\frac{\Theta}{2}\sin\frac{\Psi}{2} - \sin\frac{\Phi}{2}\sin\frac{\Theta}{2}\cos\frac{\Psi}{2} \tag{15}$$

2.4 Dynamic equations of motion

The dynamic equations of motion were obtained using momentum $\boldsymbol{\Pi}$ and angular momentum $\boldsymbol{K_0}$ change theorems, that in a noninertial frame $O_b x_b y_b z_b$ have the form [32], [33], [34]:

$$\frac{\tilde{\delta}\boldsymbol{\Pi}}{\tilde{\delta}t} + \boldsymbol{\Omega} \times \boldsymbol{\Pi} = \boldsymbol{F_b} \tag{16}$$

$$\frac{\tilde{\delta}\boldsymbol{K_0}}{\tilde{\delta}t} + \boldsymbol{\Omega} \times \boldsymbol{K_0} + \boldsymbol{V_b} \times \boldsymbol{\Pi} = \boldsymbol{M_b} \tag{17}$$

where $\boldsymbol{\Omega} = [P \quad Q \quad R]^T$ vector of quasi-angular rates, $\boldsymbol{F_b} = [X_b \quad Y_b \quad Z_b]^T$ vector of external forces expressed in $O_b x_b y_b z_b$, $\boldsymbol{M_b} = [L_b \quad M_b \quad N_b]^T$ vector of external moments with respect to point O_b, and $\frac{\tilde{\delta}}{\tilde{\delta}t}$ is local derivative. Assuming that O_b coincides with the center of mass of the quadrotor, momentum $\boldsymbol{\Pi}$ is given as:

$$\boldsymbol{\Pi} = m\boldsymbol{V_b} \tag{18}$$

where m – quadrotor mass, $\boldsymbol{V_b} = [U \quad V \quad W]^T$ – vector of quasi-velocities in $O_b x_b y_b z_b$ frame.
Angular momentum with respect to the origin of $O_b x_b y_b z_b$ frame is given as:

$$\boldsymbol{K_0} = \boldsymbol{I\Omega} \tag{19}$$

where $\boldsymbol{I}$ is inertia matrix defined as [30]:

$$\boldsymbol{I} = \begin{bmatrix} I_{xx} & -I_{xy} & -I_{xz} \\ -I_{xy} & I_{yy} & -I_{yz} \\ -I_{xz} & -I_{yz} & I_{zz} \end{bmatrix} \tag{20}$$

where I_{xx}, I_{yy}, I_{zz} are moments of inertia $O_b x_b y_b z_b$, and I_{xy}, I_{xz}, I_{yz} are products of inertia.
When (18), (19), (20) are substituted into (16) and (17) (ignoring products of inertia) the equations of motion are [35], [32], [36]:

$$m(\dot{U} + WQ - VR) = X_b \tag{21}$$

$$m(\dot{V} + UR - WP) = Y_b \tag{22}$$

$$m(\dot{W} + VP - UQ) = Z_b \tag{23}$$

$$I_x\dot{P} - (I_y - I_z)RQ = L_b \tag{24}$$

$$I_y\dot{Q} - (I_z - I_x)PR = M_b \tag{25}$$

$$I_z\dot{R} - (I_x - I_y)PQ = N_b \tag{26}$$

2.5 Forces and moments

The total external forces $\boldsymbol{F_b}$ acting on the quadrotor expressed in $O_b x_b y_b z_b$ frame are:

$$\boldsymbol{F_b} = \begin{bmatrix} X_b \\ Y_b \\ Z_b \end{bmatrix} = \boldsymbol{F_g} + \boldsymbol{F_p} + \boldsymbol{F_a} \tag{27}$$

where: $\boldsymbol{F_g}$ – gravity forces, $\boldsymbol{F_p}$ – forces from propellers, $\boldsymbol{F_a}$ – fuselage aerodynamic loads.
The total moments $\boldsymbol{M_b}$ expressed in $O_b x_b y_b z_b$ with respect to the origin O_b are:

$$\boldsymbol{M_b} = \begin{bmatrix} L_b \\ M_b \\ N_b \end{bmatrix} = \boldsymbol{M_g} + \boldsymbol{M_p} + \boldsymbol{M_a} \tag{28}$$

where: $\boldsymbol{M_g}$ – moments from gravity, $\boldsymbol{M_p}$ – moments from propellers and $\boldsymbol{M_a}$ – aerodynamics moments.

2.5.1 Gravity loads

Gravity forces $\boldsymbol{F_g}$ expressed in $O_b x_b y_b z_b$ are [37], [34], [38]:

$$\boldsymbol{F_g} = \begin{bmatrix} X_g \\ Y_g \\ Z_g \end{bmatrix} = m\boldsymbol{T_n^b} \begin{bmatrix} 0 \\ 0 \\ g \end{bmatrix} = mg \begin{bmatrix} -\sin\Theta \\ \cos\Theta\sin\Phi \\ \cos\Theta\cos\Phi \end{bmatrix} \tag{29}$$

where $\boldsymbol{T_g^b}$ is defined by (3).
It was assumed, that the origin O_b coincides with the center of mass of the object so:

$$\boldsymbol{M_g} = \begin{bmatrix} L_g \\ M_g \\ N_g \end{bmatrix} = \begin{bmatrix} 0 \\ 0 \\ 0 \end{bmatrix} \tag{30}$$

2.5.2 Loads generated by propellers

Total forces generated by four propellers are calculated as a sum of forces from individual propellers:

$$\boldsymbol{F_p} = \begin{bmatrix} X_p \\ Y_p \\ Z_p \end{bmatrix} = \boldsymbol{F_{p1}} + \boldsymbol{F_{p2}} + \boldsymbol{F_{p3}} + \boldsymbol{F_{p4}} = \sum_{j=1}^{4} \boldsymbol{F_{pj}} \tag{31}$$

where $j = \{1 \dots 4\}$ is the number of j–th propeller.
The force generated by the single propeller in $O_b x_b y_b z_b$ could be expressed as [39]:

$$\boldsymbol{F_{pj}} = \begin{bmatrix} X_{pj} \\ Y_{pj} \\ Z_{pj} \end{bmatrix} = \begin{bmatrix} 0 \\ 0 \\ -T_j \end{bmatrix} \tag{32}$$

The thrust force T_j generated by the j–th propeller is proportional to the angular rate Ω_j [40], [41], [42], [43]:

$$T_j = \rho S_p R_p^2 \Omega_j^2 k_f \tag{33}$$

where: ρ – air density, $S_p = \pi R_p^2$ – area of propeller disc, R_p – propeller radius, k_f – thrust coefficient (k_f = 1.353·10^{-4} [N/RPM^2]).
Moments generated by single j–th propeller with respect to point O_b expressed in $O_b x_b y_b z_b$ are:

$$\boldsymbol{M_{pj}} = \begin{bmatrix} L_{pj} \\ M_{pj} \\ N_{pj} \end{bmatrix} = \boldsymbol{r_{pj}} \times \boldsymbol{F_{pj}} + \begin{bmatrix} 0 \\ 0 \\ -M_j \end{bmatrix} (-1)^j = \begin{bmatrix} r_{pjx} \\ r_{pjy} \\ r_{pjz} \end{bmatrix} \times \begin{bmatrix} 0 \\ 0 \\ -T_j \end{bmatrix} + \begin{bmatrix} 0 \\ 0 \\ -M_j \end{bmatrix} (-1)^j \tag{34}$$

where $\boldsymbol{r_{pj}}$ is a vector from O_b and end in a point of mounting of the propeller. The vectors $\boldsymbol{r_{pj}}$ for each of the propellers are: $\boldsymbol{r_{p1}} = [0.108 \quad 0.139 \quad 0]^T$, $\boldsymbol{r_{p2}} = [-0.108 \quad 0.139 \quad 0]^T$, $\boldsymbol{r_{p3}} = [-0.108 \quad -0.139 \quad 0]^T$ and $\boldsymbol{r_{p4}} = [0.108 \quad -0.139 \quad 0]^T$.
Drag moment M_j of the j–th propeller is calculated as [40]:

$$M_j = \rho S_p R_p^3 \Omega_j^2 k_m \tag{35}$$

where k_m propeller drag coefficient (k_m = 7·10^{-5} [Nm/RPM^2]). The gyroscopic effects due to propellers rotations were omitted in the presented model.

2.5.3 Aerodynamic loads

Aerodynamic forces generated by the fuselage and expressed in $O_b x_b y_b z_b$ frame are defined as:

$$\boldsymbol{F_a} = \begin{bmatrix} X_a \\ Y_a \\ Z_a \end{bmatrix} = \frac{1}{2} \rho V_{tot}^2 S \begin{bmatrix} \cos\alpha\cos\beta & -\cos\alpha\sin\beta & -\sin\alpha \\ \sin\beta & \cos\beta & 0 \\ \sin\alpha\cos\beta & -\sin\alpha\sin\beta & \cos\alpha \end{bmatrix} \begin{bmatrix} C_X \\ C_Y \\ C_Z \end{bmatrix} \tag{36}$$

where: ρ – air density, V_{tot} – total flight velocity, S – reference cross-section area (assumed 0.1 [m^2]), C_X – drag force coefficient, C_Y – side force coefficient, C_Z – lift force coefficient.
Aerodynamic moments with respect to point O_b expressed in $O_b x_b y_b z_b$ are:

$$\boldsymbol{M_a} = \begin{bmatrix} L_a \\ M_a \\ N_a \end{bmatrix} = \frac{1}{2} \rho V_{tot}^2 S d \begin{bmatrix} \cos\alpha\cos\beta & -\cos\alpha\sin\beta & -\sin\alpha \\ \sin\beta & \cos\beta & 0 \\ \sin\alpha\cos\beta & -\sin\alpha\sin\beta & \cos\alpha \end{bmatrix} \begin{bmatrix} C_L + C_{LP}\dfrac{Pd}{2V_{tot}} \\ C_M + C_{MQ}\dfrac{Qd}{2V_{tot}} \\ C_N + C_{NR}\dfrac{Rd}{2V_{tot}} \end{bmatrix} \tag{37}$$

where: d – linear reference dimension (assumed 0.1 [m]), C_L – rolling moment coefficient, C_M – pitching moment coefficient, C_N – yawing moment coefficient, C_{LP} – rolling moment derivative with respect to roll rate, C_{MQ} – pitching moment derivative with respect to pitch rate, C_{NR} – yawing moment coefficient derivative with respect to yaw rate. It was assumed that aerodynamic coefficients are functions of angles of attack and sideslip.
The angle of attack α is defined as [28]:

$$\alpha = \operatorname{atan} \frac{W - W_W}{U - U_W} \tag{38}$$

In the numerical implementation the function $\operatorname{atan2}(W - W_W, U - U_W)$ was used to ensure the values of α from –180° up to 180°.
The angle of sideslip β is [28]:

$$\beta = \operatorname{asin} \frac{V - V_W}{V_{tot}} \tag{39}$$

Total flight velocity with respect to the oncoming flow V_{tot} is calculated as:

$$V_{tot} = \sqrt{(U - U_W)^2 + (V - V_W)^2 + (W - W_W)^2} \tag{40}$$

where U_w, V_W, W_W are linear wind velocities in the body-fixed frame $O_b x_b y_b z_b$. Lookup table methodology was used to implement fuselage aerodynamic coefficients as functions of two inflow angles.

2.5.4 Control inputs mixer

Outputs from each autopilot channel were mixed to calculate the total angular speed for each propeller:

$$\begin{bmatrix} \Omega_{1c} \\ \Omega_{2c} \\ \Omega_{3c} \\ \Omega_{4c} \end{bmatrix} = \begin{bmatrix} 1 & 1 & 1 & 1 \\ 1 & 1 & -1 & -1 \\ 1 & -1 & -1 & 1 \\ 1 & -1 & 1 & -1 \end{bmatrix} \begin{bmatrix} U_1 \\ U_2 \\ U_3 \\ U_4 \end{bmatrix} \tag{41}$$

where: U_1 is the control signal (angular rate of the motor) from altitude autopilot, U_2 is commanded signal from roll autopilot, U_3 is the signal from pitch autopilot and U_4 is the commanded value from yaw autopilot. The altitude change is realized by changing the speed of propellers by the same amount. The differences between propeller angular rates result in thrust variations and quadcopter attitude changes. Proportional-integral-derivative (PID) controllers were used for each channel. The autopilot structure is not discussed here because is out of the scope of the presented study.

2.6 Electric motor model

It was assumed that all four brushless direct-current (BLDC) motors are the same. Each of the motors was modeled using the first-order transfer function:

$$\Omega_j = \frac{1}{T_s s + 1} \Omega_{jc} \tag{42}$$

where: Ω_{jc} – commanded angular rate (obtained from (41)), T_s – time constant (it was assumed 0.05 s). The upper saturation of angular speed was included in the model. It was found experimentally that the maximum achievable propeller angular speed for the tested DJI Mavic 2 Pro drone is 98000 RPM.

2.7 Wind model

The total wind velocity expressed in $O_n x_n y_n z_n$ coordinate frame is V_{Wtot}, and the direction of the oncoming wind is defined by the angle Ψ_W (clockwise when looking from the top, e.g. 90° means wind from east). The wind velocities in $O_n x_n y_n z_n$ frame are:

$$\begin{bmatrix} U_{Wn} \\ V_{Wn} \\ W_{Wn} \end{bmatrix} = \begin{bmatrix} -V_{Wtot} \cos \Psi_W \\ -V_{Wtot} \sin \Psi_W \\ 0 \end{bmatrix} \tag{43}$$

Next, the wind velocities U_{Wn}, V_{Wn}, W_{Wn} are transformed from $O_n x_n y_n z_n$ to body-fixed frame $O_b x_b y_b z_b$:

$$\begin{bmatrix} U_W \\ V_W \\ \mathrm{W_W} \end{bmatrix} = \begin{bmatrix} \cos\Theta\cos\Psi & \sin\Phi\sin\Theta\cos\Psi - \cos\Phi\sin\Psi & \cos\Phi\sin\Theta\cos\Psi + \sin\Phi\sin\Psi \\ \cos\Theta\sin\Psi & \sin\Phi\sin\Theta\sin\Psi + \cos\Phi\cos\Psi & \cos\Phi\sin\Theta\sin\Psi - \sin\Phi\cos\Psi \\ -\sin\Theta & \sin\Phi\cos\Theta & \cos\Phi\cos\Theta \end{bmatrix}^{\mathrm{T}} \begin{bmatrix} U_{Wn} \\ V_{Wn} \\ W_{Wn} \end{bmatrix} \tag{44}$$

2.8 Energy consumption model

The test platform is equipped with a single Lithium-Polymer, rechargeable, four-cell battery. This kind of battery offers high energy density, a high rate of charge/discharge, and relatively low cost [44]. The onboard battery parameters declared by the Manufacturer are listed in
Table 1.

Table 1 – Battery parameters [26].

Parameter	Value
Capacity	3850 mAh
Voltage	15.4 V
Max Charging Voltage	17.6 V
Battery Type	LiPo 4S
Energy	59.29 Wh
Net Weight	297 g
Charging Temperature Range	From 5℃ to 40℃
Max Charging Power	80 W

Theoretically, the amount of energy available onboard is 15.4 [V] · 3.85 [Ah] = 59.29 [Wh]. For the fully charged battery, the flight endurance is approximately 31 min (value declared by the Manufacturer).
The total energy consumption E_c is a sum of two components: energy consumed by all four electric motors E_m and energy used by onboard systems and sensors other than motors E_s [3], [45]:

$$E_c = E_m + E_s \tag{45}$$

Energy used on propulsion E_m is often a way higher than on onboard systems E_s [10].
Energy consumed by all four motors could be calculated as [46], [47], [48], [48]:

$$E_m = \int_{t_0}^{t_k} \sum_{j=1}^{4} U_j(t) I_j(t)\, dt \tag{46}$$

where: $U_j(t)$ – voltage of j–th motor, $I_j(t)$ – electric current on j–th motor, t_0 – initial time (in most cases 0 s), t_k – total quadrotor flight time, $j = \{1,2,3,4\}$ – motor number. The values of current were not measured directly by onboard equipment, so it was needed to express (46) in terms of motor speed instead of current.
Energy E_m consumed by all electric motors could be written as [4]:

$$E_m = \int_{t_0}^{t_k} \sum_{j=1}^{4} \tau_j(t) \Omega_j(t)\, dt \tag{47}$$

where: $\tau_j(t)$ – moment of the j–th motor, $\Omega_j(t)$ – angular speed of the j–th motor, $j = \{1,2,3,4\}$ – motor number.
Equation (47) could be transformed to [4]:

$$E_m = \int_{t_0}^{t_k} \sum_{j=1}^{4} \left(I_{zzp} \dot{\Omega}_j(t) + k_m \Omega_j^2(t) + D_v \Omega_j(t) \right) \Omega_j(t) dt \tag{48}$$

where: I_{zzp} – propeller moment of inertia with respect to its rotation axis (3.21322·10^{-5} [kgm^2]), k_m – drag coefficient of the propeller, D_v – viscous damping coefficient of the motor. Dot symbol above some quantities means the first derivative with respect to time, for example $\dot{\Omega}_j(t) = \frac{\partial\Omega_j(t)}{\partial t}$.
To increase the model fidelity a motor efficiency was included in the equations [4]:

$$E_m = \int_{t_0}^{t_k} \sum_{j=1}^{4} \frac{I_{zzp}\dot{\Omega}_j(t) + k\Omega_j^2(t) + D_v\Omega_j(t)}{f_{r,j}\left(\tau_j(t), \Omega_j(t)\right)} \Omega_j(t)dt \tag{49}$$

where: $f_{r,j}$ – efficiency of the j–th electric motor. It was assumed that $f_{r,j}$ = 0.94.
In some works, e.g. [3] the Authors suggests omitting $D_v\Omega_j^2(t)$ and in this way (49) is simplified to:

$$E_m = \int_{t_0}^{t_k} \sum_{j=1}^{4} \frac{I_{zzp}\dot{\Omega}_j(t) + k\Omega_j^2(t)}{f_{r,j}\left(\tau_j(t), \Omega_j(t)\right)} \Omega_j(t)dt \tag{50}$$

The total energy consumed by onboard subsystems was calculated as:

$$E_s = \int_{t_0}^{t_k} E_{sub}\, dt \tag{51}$$

where E_{sub} – instantaneous power consumption. The value of E_{sub} was obtained experimentally. The stationary tests were conducted. During measurements, the drone was powered but all four electric motors were switched off and the discharge rate was observed. The initial state of charge was 97% and the final state of charge was 15%. The discharge time was 150 minutes. From obtained data, it was calculated that onboard systems and sensors consume approximately E_{sub} = 23.7 [J/s].
It was assumed that the battery is a new one and free from manufacturing errors. The aging effects were omitted in the model. The influence of temperature on the battery capacity was neglected [50].
Battery state of charge could be defined as [3], [51]:

$$SOC = SOC_0 - \int_0^t \frac{I}{Q_{batt}} dt \tag{52}$$

where: I – electric current, SOC_0 – initial battery state of charge, Q_{batt} – battery capacity. For fully charged battery the SOC = 100%, and for fully discharged 0%.
To calculate the voltage during the battery discharge process the Shepherd model was used. This model is widely used to describe the battery dynamics [52], [53], [52], [54], [55], [56], [57]:

$$U_{disch} = E_0 - K\frac{Q}{Q - \int_0^t Idt} I + Ae^{-B\int_0^t Idt} - RI \tag{53}$$

where: U_{disch} – battery voltage, E_0 – open circuit voltage of the battery, K – polarization resistance coefficient, Q – battery capacity, t – time, I – current, A – amplitude in the exponential zone, B – time constant inverse in the exponential zone, R – internal battery resistance (it was assumed 0.1 [Ω]). Constants A = 0.2 [V] and B = 6.1 [Ah]$^{-1}$ were obtained according to [58].

3. Results

The developed model was implemented into MATLAB/Simulink 2020b. The equations of motion were integrated using a fixed step Runge-Kutta solver with step size 0.001 s. Simulation takes place on the laptop computer with Procesor Intel(R) Core(TM) i7-8750H CPU @ 2.20GHz and 16 GB RAM.
A series of 14 flight tests were evaluated on 20/21 May 2021 in Przasnysz airfield (Latitude 53.0050011, Longitude 20.9383297) in Poland to validate the developed model. Flight tests were realized mainly in the P-mode of the autopilot (that setting limits the drone maneuverability) and

partially using the manual control. The flight data parameters were registered using only build-in functionality without additional sophisticated equipment because adding some onboard measurement devices could increase the mass of the drone and significantly reduce the performance. The experimental data sampling frequency was 10 Hz. Linear accelerations and angular rates were not recorded during flight trials which complicate the validation process significantly. The resulting flight logs were analyzed offline using Airdata online service [59] and then imported into MATLAB to compare with simulation results. Initial conditions to the simulation were set the same as derived from flight logs. Validation takes place after completing the test campaign.
One of the flight tests (case number May-20th-2021-12-06PM-Flight-Airdata) was presented here to illustrate the validation results. Mean wind speed in the analyzed case was 6.5 m/s and mean wind azimuth 301° (these values were measured on the airfield using an anemometer and estimated later from the obtained flight logs).
In Figure 3 the drone flight parameters obtained from the simulation are presented.

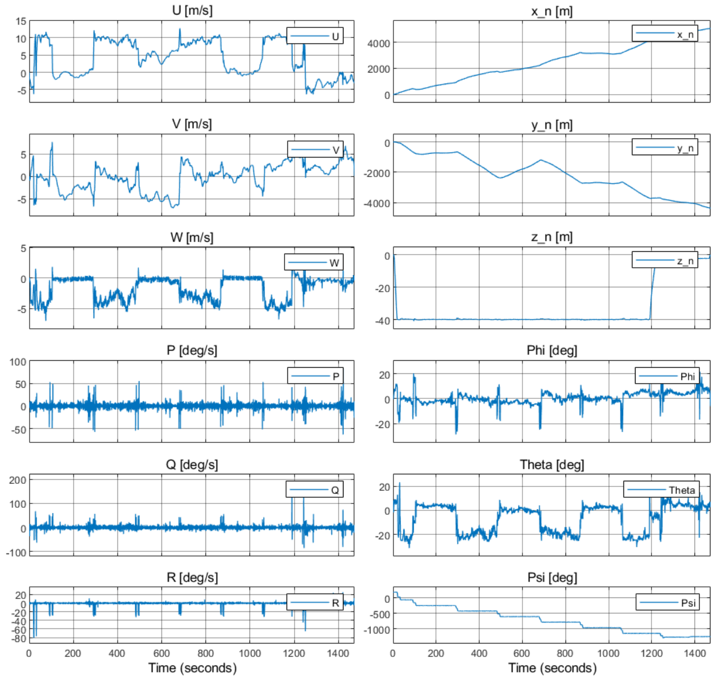

Figure 3 – Quadrotor flight parameters (simulation only).

In Figure 4 a, b, c the comparison of Euler angles obtained from the flight test and numerical simulation is shown. In Figure 4 d the altitude comparison is shown.

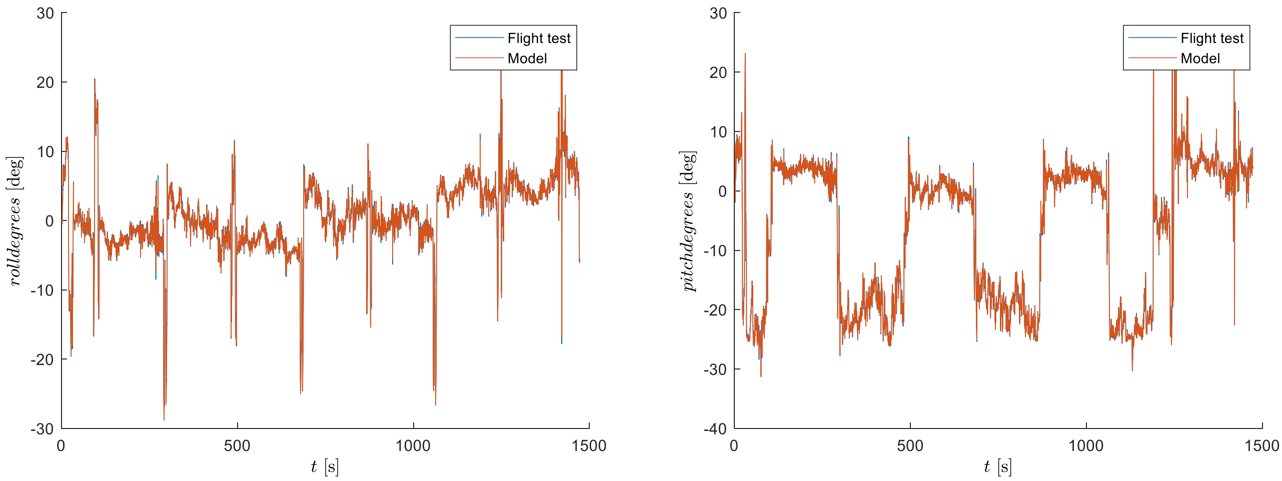

(a) (b)

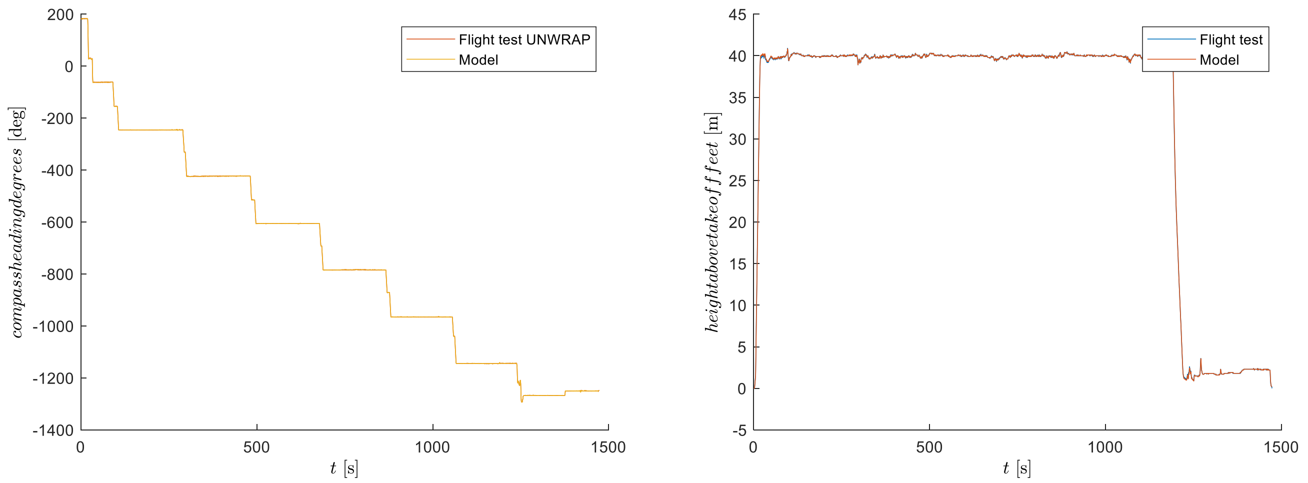

(c) (d)

Figure 4 – Euler angles and altitude comparison.

The total flight time was 1500 [s]. Roll and pitch angles are oscillatory due to air turbulence. Yaw angle decreases up to –1300°. It means that the object realized left turns (looking from aft) several times.

At the beginning of the flight, the altitude increases from 0 [m] to 40 [m]. Then the drone realizes most of the mission at attitude 40. In 1200 [s] the altitude decreases rapidly to 2 [m] and hold constant nearly to the end of the flight. Finally, the drone landed and the attitude drops to 0 [m]. The experimental results match the simulation predictions accurately.

In Figure 5 the propeller speed time history obtained from simulation is presented. Propeller angular rates were not measured during the flight, so it was impossible to compare them with the model.

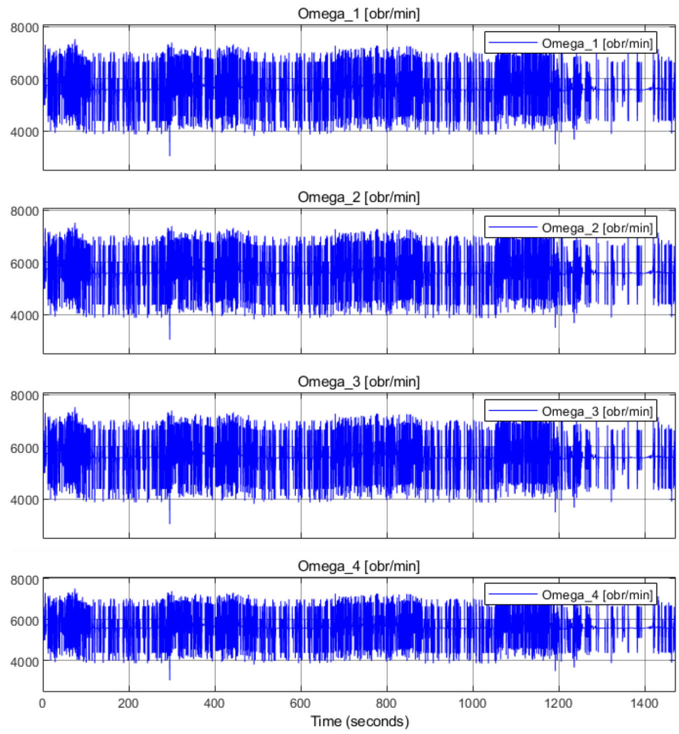

Figure 5 – Propellers angular speed obtained from simulation.

With the aim of the simulation, it was predicted that the propeller minimum speed achieved during tests was approximately 4000 RPM and a maximum 7700 RPM.

In Figure 6 the comparison of the amount of energy consumed by the quadrotor is shown.

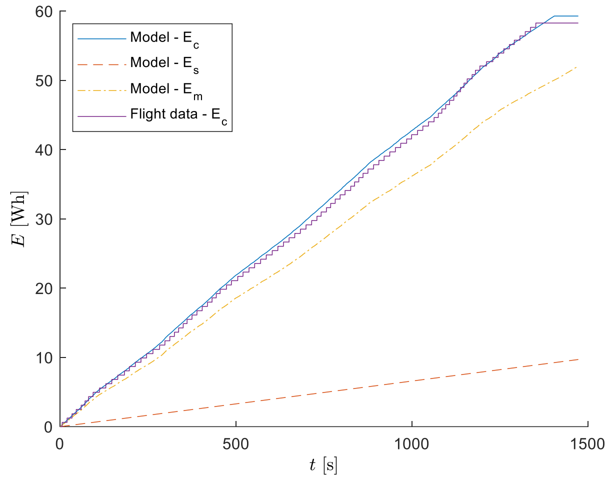

Figure 6 – Energy consumed by the quadrotor (experiment vs simulation).

The experimental results match well the numerical predictions of total energy consumption E_c. From the simulation results, it might be concluded that the total energy consumed by the subsystems E_s was approximately 9 [Wh] (5 times less than energy spent on propulsion).
In Figure 7 the battery state of charge comparison between flight trials and simulation is presented. The state of charge during experiments was recorded with a sensor resolution 1%.

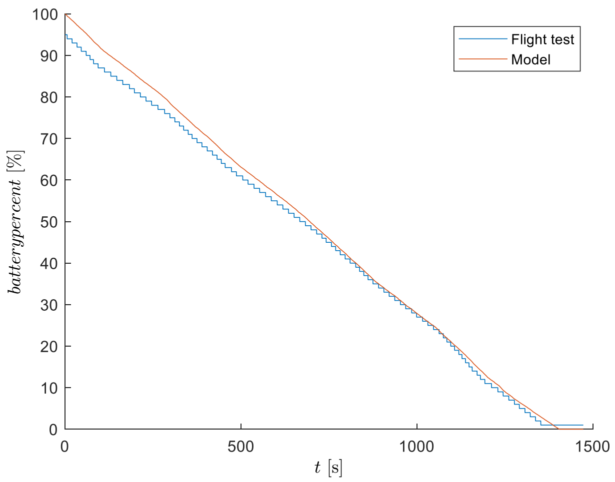

Figure 7 – Battery state of charge comparison.

The initial state of charge was 97%. The curve decreases linearly. At the end of the real flight state of charge was 1%. Tests results agree with model predictions accurately.
In Figure 8 the battery voltage was presented (total and on individual battery cells).

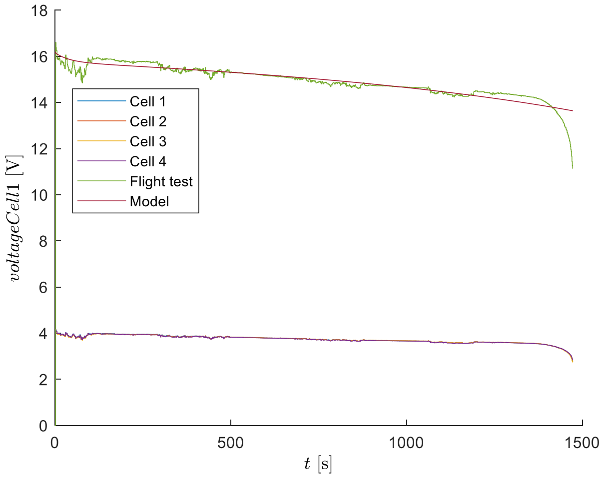

Figure 8 – Battery voltage.

The total voltage is a sum of voltages from individual cells. A typical discharge curve for a lithium-polymer battery was obtained. The voltage of a fully charged device is higher than the discharged one. At the beginning of the flight, the total voltage is approximately 16 [V] and decreases slowly with time. At the end of the mission, the total voltage rapidly decreases to 12 [V]. The curves of voltage for each cell coincide with each other.

4. Discussion and Conclusions

In this paper, the nonlinear mathematical model of the quadrotor was developed and validated. The modified DJI MAVIC 2 Pro drone was used as a test platform. The experimental data correlates with the results of numerical simulation. The obtained model could be used to predict the drone flight parameters and energy consumption during the mission. Flight tests take place in windy conditions. The wind effect is one of the main difficulties to predict accurately the object behavior. Presented study extends the work of Yacef et all. [3], [4] because calculations for the whole mission are shown and partially fills the literature gap. Energy consumed by propellers is several times higher when compared to energy spent on the operation of other onboard subsystems.

Future works might concentrate on flight tests to gather more data and increase the reliability of the model. The propulsion model could be improved to include various aerodynamic phenomena. Wind tunnel tests of the isolated fuselage of the drone might be evaluated to improve the aerodynamic coefficients database. Additional lightweight onboard instrumentation might be considered to increase the availability of the flight parameters registered during the flight. Also, precise wind measurements might be conducted during the flight tests to understand the atmospheric conditions.

5. Copyright Statement

6. Acknowledgments

This research was supported by National Center for Research and Development (NCBiR) [grant number 4/1.1.1/2020 „Renewable Energy Sources (RES) in transport”].

Special thanks to Marcin Kasprzyk for conducting the flight trials.

Notation
The following symbols and abbreviations are used in this manuscript:
Latin symbols

A	amplitude in the exponential zone, [V]
B	time constant inverse in the exponential zone, $[\text{Ah}]^{-1}$
C_L, C_M, C_N	rolling, pitching and yawing moments coefficients, [-]
C_{LP}, C_{MQ}, C_{NR}	roll, pitch and yaw damping moments coefficients, [-]
C_X, C_Y, C_Z	drag, side, and lift force coefficients, [-]
d	linear reference dimension, [m]
D_v	viscous damping coefficient of the motor, [Nms/rad]
e_0, e_1, e_2, e_3	quaternion elements, [-]
E	quaternion norm, [-]
E_c	total energy consumed by the quadrotor, [Wh]
E_m	energy consumed by all the four electric motors, [Wh]
E_s	energy consumed by onboard subsystems, [Wh]
E_{sub}	instantaneous power consumption by the subsystems, [W]
$f_{r,j}$	the efficiency of the j-th electric motor, [–]
$I_j(t)$	current, [A]
I_{zzp}	propeller moment of inertia, [kgm^2]
$\boldsymbol{F_a}$	aerodynamic forces, [N]
$\boldsymbol{F_b}$	total forces in the body-fixed frame $O_b x_b y_b z_b$, [N]
$\boldsymbol{F_g}$	gravity forces, [N]
$\boldsymbol{F_p}$	forces generated by the propellers, [N]
$\boldsymbol{F_{pj}}$	force generated by j-th the propeller, [N]
g	gravity acceleration, [m/s^2]
h	altitude, [m]
h_{int}	numerical integration step, [s]
$\boldsymbol{I}$	inertia matrix, [kgm^2]
I_{xx}, I_{yy}, I_{zz}	moments of inertia, [kgm^2]
I_{xy}, I_{yz}, I_{xz}	products of inertia, [kgm^2]
j = {1,2,3,4}	number of the propeller, [–]
k	coefficient which drives the norm of the quaternion state vector to 1.0, [-]
k_f	propeller thrust coefficient, [N/RPM^2]
k_m	propeller drag coefficient, [Nm/RPM^2]
K_0	angular momentum, [kgm^2/s]
L_b, M_b, N_b	rolling, pitching, and yawing moment in the body-fixed frame $O_b x_b y_b z_b$ with respect to the center of mass, [Nm]
L_g, M_g, N_g	rolling, pitching, and yawing moment from gravity in the body-fixed frame $O_b x_b y_b z_b$ with respect to the center of mass, [Nm]
m	quadrotor mass, [kg]
$\boldsymbol{M_a}$	aerodynamic moments, [Nm]
$\boldsymbol{M_b}$	total moments in the body-fixed frame $O_b x_b y_b z_b$, [Nm]
$\boldsymbol{M_g}$	moments due to gravity, [Nm]
$\boldsymbol{M_p}$	moments due to propellers, [Nm]
$\boldsymbol{M_{pj}}$	moment generated by the j-th propeller, [Nm]
M_j	drag moment of the j-th propeller, [Nm]
P, Q, R	quasi-angular rates in the body-fixed frame $O_b x_b y_b z_b$, [°/s]
P_c, Q_c, R_c	commanded roll, pitch and yaw rates, [°]
P_e, Q_e, R_e	roll, pitch and yaw angular rates tracking error, respectively, [°/s]
Q_{batt}	battery capacity, [Wh] or [Ah]
$\boldsymbol{r_{pj}}$	vector of the position of j–th propeller, [m]
R	internal battery resistance, [Ω]
R_p	propeller radius, [m]
S	fuselage cross-section area, [m^2]
SOC	state of charge of the battery, [%]
SOC_0	initial state of charge of the battery, [%]

S_p	propeller disc area, [m^2]
t	time, [s]
t_0	initial time, [s]
t_k	time of flight of the quadrotor, [s]
$\boldsymbol{T_b^n}$	transformation matrix from the body-fixed frame $O_b x_b y_b z_b$ to navigation frame $O_n x_n y_n z_n$
T_s	electric motor time constant, [s]
T_j	thrust force generated by the j-th propeller, [N]
U_1, U_2, U_3, U_4	control inputs, [°/s]
U, V, W	linear quasi-velocities in the body-fixed frame $O_b x_b y_b z_b$, [m/s]
$U_j(t)$	voltage of the j-th electric motor, [V]
U_W, V_W, W_W	linear wind velocities in the body-fixed frame $O_b x_b y_b z_b$, [m/s]
U_{Wn}, V_{Wn}, W_{Wn}	linear wind velocities in the navigation frame $O_n x_n y_n z_n$, [m/s]
$\boldsymbol{V_b}$	vector of quasi-velocities in $O_b x_b y_b z_b$ frame, [m/s]
V_{tot}	total flight velocity with respect to air, [m/s]
V_{Wtot}	wind total velocity, [m/s]
W_n	vertical velocity in the navigation frame $O_n x_n y_n z_n$, [m/s]
x_n, y_n, z_n	center of mass coordinates in the navigation frame $O_n x_n y_n z_n$, [m]
$\boldsymbol{x_{state}}$	the state vector of the system,
X_a, Y_a, Z_a	total axial, side, and normal aerodynamic force in the body-fixed frame $O_b x_b y_b z_b$, [N]
X_b, Y_b, Z_b	total axial, side, and normal force in the body-fixed frame $O_b x_b y_b z_b$, [N]
X_g, Y_g, Z_g	axial, side, and normal force from gravity in the body-fixed frame $O_b x_b y_b z_b$, [N]
X_p, Y_p, Z_p	axial, side, and normal force from propulsion in the body-fixed frame $O_b x_b y_b z_b$, [N]

Greek symbols

α	angle of attack, [°]
β	angle of sideslip, [°]
Φ, Θ, Ψ	roll, pitch, and yaw angles, respectively, [°]
Φ_c, Θ_c, Ψ_c	commanded roll, pitch, and yaw angles, [°]
Φ_e, Θ_e, Ψ_e	roll, pitch, and yaw tracking error, respectively, [°]
$\boldsymbol{\Lambda}$	transformation matrix from the body-fixed frame $O_b x_b y_b z_b$ to the navigation frame $O_n x_n y_n z_n$
ρ	air density, [kg/m^3]
$\tau_j(t)$	moment on j–th motor, [Nm]
Ψ_W	wind azimuth, [°]
$\boldsymbol{\Omega}$	vector of quasi-angular rates in the body-fixed frame $O_b x_b y_b z_b$, [°/s]
Ω_j	angular rate of the j–th propeller, [°/s]
Ω_{jc}	commanded angular rate of the j–th propeller, [°/s]
$\boldsymbol{\Pi}$	momentum, [kg·m/s]

Abbreviations

BLDC	Brushless Direct Current
DOF	Degree of Freedom
ISA	International Standard Atmosphere
PID	Proportional-integral-derivative
RPM	Revolutions per Minute
WGS	World Geodetic System

References

[1] He Z and Zhao L. A Simple Attitude Control of Quadrotor Helicopter Based on Ziegler-Nichols Rules for Tuning PD Parameters. *The Scientific World Journal*, pp. 1–13, 2014.

[2] Jimenez P, Lichota P, Agudelo D and Rogowski K. Experimental Validation of Total Energy Control System for UAVs. *Energies,* Vol. 13(1), No. 14, pp. 1–18, 2020.

[3] Yacef F, Rizoug N and Degaa L. Energy-Efficiency Path Planning for Quadrotor UAV Under Wind Conditions. In 2020 7th International Conference on Control, Decision and Information Technologies (CoDIT), Prague, Czech Republic, 29 June–2 July 2020.

[4] Yacef F, Rizoug N, Degaa L, Bouhali O and Hamerlain M. Trajectory Optimisation for a Quadrotor Helicopter Considering Energy Consumption. In 2017 4th International Conference on Control, Decision and Information Technologies (CoDIT), Barcelona, Spain, 5–7 April 2017.

[5] Sheng S and Sun C. Control and Optimization of a Variable-Pitch Quadrotor with Minimum Power Consumption. *Energies,* Vol. 9(4), No. 232, pp.1–18, 2016.

[6] Agarwal V and Tewari R R. Improving Energy Efficiency in UAV Attitude Control using Deep Reinforcement Learning. *Journal of Scientific Research,* Vol. 65, No. 3, pp. 209–219, 2021.

[7] Shivgan R and Dong Z. Energy-Efficient Drone Coverage Path Planning using Genetic Algorithm. In 2020 IEEE 21st International Conference on High Performance Switching and Routing (HPSR), Newark, NJ, USA, 11–14 May 2020.

[8] Pradeep P, Park S G and Wei P. Trajectory Optimization of Multirotor Agricultural. In 2018 IEEE Aerospace Conference, Big Sky, MT, USA, 3–10 March 2018.

[9] Jee S and Cho H. Comparing Energy Consumption following Flight Pattern for Quadrotor. *Journal of IKEEE,* Vol. 22, No. 3, pp. 747–753, 2018.

[10] Gao N, Zeng Y, Wang J, Wu D, Zhang C, Song Q, Qian J and Jin S. Energy Model for UAV Communications: Experimental Validation and Model Generalization. *China Communications,* Vol. 18, No. 7, pp. 253–264, 2021.

[11] Dietrich T, Krug S and Zimmermann A. An Empirical Study on Generic Multicopter Energy Consumption Profiles. In *11th IEEE Int. Systems Conference (SysCon 2017)*, Montreal, QC, Canada, 2017.

[12] Abeywickrama H V, Jayawickrama B A, He Y and Dutkiewicz E. Empirical Power Consumption Model for UAVs. 2018 IEEE 88th Vehicular Technology Conference (VTC-Fall), Chicago, IL, USA, 27–30 August 2018.

[13] Korneyev A, Gorobetz M, Alps I and Ribickis L. Adaptive Traction Drive Control Algorithm for Electrical Energy Consumption Minimisation of Autonomous Unmanned Aerial Vehicle. Electrical, Control and Communication Engineering, Vol. 15, No. 2, pp. 62–70, 2019.

[14] Hwang M-h, Cha H-R and Jung S Y. Practical Endurance Estimation for Minimizing Energy Consumption of Multirotor Unmanned Aerial Vehicles. Energies, Vol. 11(9), No. 2221, pp. 1–11, 2018.

[15] Wang Y, Wang Y and Ren B. Energy Saving Quadrotor Control for Field Inspection. IEEE Transactions on Systems, Man, and Cybernetics: Systems (Early Access), 2020.

[16] Aleksandrov D and Penkov I. Energy Consumption of Mini UAV Helicopters with Different Number of Rotors, pp. 259–262, 2012.

[17] Chen Y, Baek D, Bocca A, Macii A, Macii E and Poncino M. A Case for a Battery-Aware Model of Drone Energy Consumption. 2018 IEEE International Telecommunications Energy Conference (INTELEC), Turino, Italy, 7–11 October 2018

[18] Apeland J, Pavlou D and Hemmingsen T. Suitability Analysis of Implementing a Fuel Cell on a Multirotor Drone, Journal of Aerospace Technology and Management, Vol. 12, pp. 1–14, 2020.

[19] Prasetia A S, Wai R-J, Wen Y-L and Wang Y-K. Mission-Based Energy Consumption Prediction of Multirotor UAV. IEEE Access, Vol. 7, pp. 33055–33063, 2019.

[20] Rodrigues T A, Patrikar J, Choudhry A, Feldgoise J, Arcot V, Gahlaut A, Lau S, Moon B, Wagner B, Matthews H S, Scherer S and Samaras C. In-flight positional and energy use data set of a DJI Matrice 100 quadcopter for small package delivery. *Sci Data,* 155, pp. 1–8, 2021.

[21] Roberts J F, Zufferey J-C and Floreano D. Energy Management for Indoor Hovering Robots. In 2008 IEEE/RSJ International Conference on Intelligent Robots and Systems, Nice, France, 22–26 September 2008.

[22] Chan C W and Kam T Y. A procedure for power consumption estimation of multi-rotor unmanned aerial vehicle. Journal of Physics: Conference Series, 1509, 2020.

[23] Abdilla A, Richards A and Burrow S. Power and Endurance Modelling of Battery-Powered Rotorcraft. In *2015 IEEE/RSJ International Conference on Intelligent Robots and Systems (IROS)*, Hamburg, Germany, 28 September–2 October 2015.

[24] Penkov I and Aleksandrov D. Analysis and study of the influence of the geometrical parameters of mini unmanned quad-rotor helicopters to optimise energy saving. *International Journal of Automotive and Mechanical Engineering*, Vol. 14, No. 4, pp. 4730–4746, 2017.

[25] [Online]. https://www.dji.com/pl/mavic-2/info, [13 July 2021].

[26] National Aeronautics and Space Administration, U.S. Standard Atmosphere, 1976, Washington, D.C., 1976.

[27] Zipfel P. *Modeling and Simulation of Aerospace Vehicle Dynamics*. American Institute of Aeronautics and Astronautics, Inc.: Reston, Virginia, USA, 2000.

[28] Allerton D. *Principles of Flight Simulation*. John Wiley & Sons: Wiltshire, 2009.

[29] Stevens B L, Lewis F L and Johnson E N. *Aircraft Control and Simulation. Dynamics, Controls Design, and Autonomous Systems*. John Wiley & Sons, Inc.: New York, USA, 2016.

[30] Dreier M. *Introduction to Helicopter and Tiltrotor Simulation*. American Institute of Aeronautics and Astronautics: Reston, VA, USA, 2007.

[31] Lichota P, Dul F and Karbowski A. System Identification and LQR Controller Design with Incomplete State Observation for Aircraft Trajectory Tracking. *Energies,* 2020, pp. 1–27.

[32] Phillips W. *Mechanics of Flight*, John Wiley & Sons: Hoboken, New Jersey, USA, 2004.

[33] Gudmundsson S. *General Aviation Aircraft Design – Applied Methods and Procedures*. Elsevier: Amsterdam, 2012.

[34] Thomson W T. *Introduction to Space Dynamics*. Dover Publications, Inc.: New York, USA, 1961.

[35] Etkin B. *Dynamics of Atmospheric Flight*, John Wiley & Sons: New York, USA, 1972.

[36] Abzug M. *Computational Flight Dynamics*. American Institute of Aeronautics and Astronautics, Inc.: Reston, VA, USA, 1998.

[37] Phang S K, Cai C, Chen B M and Lee T H. Design and Mathematical Modeling of a 4-Standard-Propeller (4SP) Quadrotor. In Proceedings of the 10th World Congress on Intelligent Control and Automation, Beijing, China, 6–8 July 2012.

[38] Sanketi J, Kasliwal R, Raghavan S and Awan S. Modelling and Simulation of a Multi-Quadcopter Concept. *International Journal of Engineering Research & Technology (IJERT)*, Vol. 5, No. 10, 2016.

[39] Salma N M and Osman K. Modelling and PID control system integration for quadcopter DJIF450 attitude stabilization. *Indonesian Journal of Electrical Engineering and Computer Science* 2020*, Vol.* 19, No. 3, pp. 1235–1244.

[40] Pounds P, Mahony R and Corke P. Modelling and Control of a Large Quadrotor Robot. *Control Engineering Practice,* Vol. 18, No. 7, pp. 691–699, 2010.

[41] Benić Z, Piljek P and Kotarski D. Mathematical Modelling of Unmanned Aerial Vehicles with Four Rotors, *Interdisciplinary Description of Complex Systems XXX,* 14(1), pp. 88–100.

[42] Salameh I M, Ammar E M and Tutunji T A. Identification of Quadcopter Hovering Using Experimental Data. 2015 IEEE Jordan Conference on Applied Electrical Engineering and Computing Technologies (AEECT). Amman, Jordan, 3–5 November 2015.

[43] Yacef F, Bouhali O, Hamerlain M and Rizoug N. Observer-based Adaptive Fuzzy Backstepping Tracking Control of Quadrotor Unmanned Aerial Vehicle Powered by Li-ion Battery. *Journal of Intelligent and Robotic Systems,* pp. 179–197, 2016.

[44] Jaafar W and Yanikomeroglu H, Dynamics of Quadrotor UAVs for Aerial Networks: An Energy Perspective.

[45] Morbidi F, Cano R and Lara D. Minimum-Energy Path Generation for a Quadrotor UAV. In 2016 IEEE International Conference on Robotics and Automation (ICRA), Stockholm, Sweden, 16–21 May 2016.

[46] Fouad Y, Rizoug N, Bouhali O and Hamerlain M. Optimization of Energy Consumption for Quadrotor UAV. In International Micro Air Vehicle Conference and Flight Competition (IMAV) 2017, Toulouse, France, 2017.

[47] Pradeep P and Wei P. Energy Efficient Arrival with RTA Constraint for Multirotor eVTOL in Urban Air Mobility. *Journal of Aerospace Information Systems,* Vol. 16, No. 7, pp. 1–15, 2019.

[48] Morbidi F and Pisarski D. Practical and Accurate Generation of Energy-Optimal Trajectories for a Planar Quadrotor. 2021 IEEE International Conference on Robotics and Automation (ICRA), Xi'an, China, 30 May–5 June 2021.

[49] Mesbahi T, Rizoug N, Bartholomeus P and Moigne P L. Li-ion Battery Emulator for Electric Vehicle Applications. In 2013 IEEE Vehicle Power and Propulsion Conference (VPPC), Beijing, China, 15–18 October 2013.

[50] Li F, Song W-P, Song B-F and Zhang H, Dynamic modeling, simulation, and parameter study of electric quadrotor system of Quad-Plane UAV in wind disturbance environment. *International Journal of Micro Air Vehicles,* Vol. 13, pp. 1–23, 2021.

[51] Tremblay O and Dessaint L-A. Experimental Validation of a Battery Dynamic Model for EV Applications. *World Electric Vehicle Journal,* Vol. 3, pp. 289–298, 2009.

[52] Mousavi S M and Nikdel M. Various battery models for various simulation studies and applications, *Renewable and Sustainable Energy Reviews,* Vol. 32, pp. 477–485, 2014.

[53] Azam S M, Battery Identification, Prediction and Modelling (Master Thesis), Colorado State University, Fort Collins, Colorado, 2018.

[54] Raszmann E, Baker K, Shi Y, and Christensen D. Modeling Stationary Lithium-Ion Batteries for Optimization and Predictive Control. 2017 IEEE Power and Energy Conference at Illinois (PECI), Champaign, IL, USA, 23–24 February 2017.

[55] Hemi H, M'Sirdi N K and Naamane A. A New Proposed Shepherd Model of a Li-Ion Open Circuit Battery Based on Data Fitting. In *IMAACA 2019*, Lisbon, Portugal, 2019.

[56] [Online]. Available: https://www.mathworks.com/help/physmod/sps/powersys/ref/battery.html. [9 October 2021].

[57] Hinz H., Comparison of Lithium-Ion Battery Models for Simulating Storage Systems in Distributed Power Generation, *Inventions,* 2019.

[58] [Online]. Available: https://airdata.com